

MULTISCALE ANALYSIS OF PRESTRESSED CONCRETE STRUCTURES

Arturo Moyeda^{1,2,*} & Jacob Fish¹

¹Columbia University, New York, US

²Constructora Moyeda, Monterrey, México

*Address all correspondence to: Arturo Moyeda, 500 W. 120th St., 610 Mudd, Columbia University, New York 10027, USA; Tel.: +1 212 854 3143; Fax: +1 212 854 6267, E-mail: am3777@columbia.edu

Original Manuscript Submitted: 7/7/2018; Final Draft Received: 7/7/2018

A multiscale beam element for the analysis of prestressed concrete that accounts for the initial effects of prestressing, creep, shrinkage, and temperature was developed within the framework of the reduced order computational continua (RC²), which accounts for representative volume elements (RVEs) of finite size. A constitutive law rescaling approach for the multiscale beams that renders the formulation nearly invariant to the beam element length was developed. The proposed rescaling approach differs from the classical rescaling for continuum elements where the constitutive laws are rescaled by a factor linearly proportional to the characteristic element size. The multiscale beam element formulation has been validated against several experiments.

KEY WORDS: multiscale, concrete, beam, prestressed

1. INTRODUCTION

Civil engineering structures, such as bridges and buildings, are commonly analyzed using three-dimensional beam elements. This approach is an easy pathway for model generation and postprocessing that provides member forces employed in traditional design. On the other hand, analysis of concrete structures using three-dimensional continuum elements that accounts for material non-linearities (Mohr et al., 2010) is quite rare and is reserved for special applications due to the need for intensive computations.

Being one of the most important and commonly used construction materials, concrete has been the subject of study since the beginning of the last century. Numerous material models for concrete have been developed, including but limited to damage models (Willam and Warnke, 1974; Pijaudier-Cabot and Mazars, 2001), plasticity models (Lee and Fenves, 1998), creep and shrinkage models employed in the design code (fib CEB-FIP, 2010; AASHTO, 2014), and a combination of damage and plasticity models (Bazant et al., 2000; Cervenka and Cervenka, 2008; Grassl et al., 2013) just to mention a few.

Reinforced concrete beam elements that account for nonlinearity of steel and concrete have been developed, including a fiber-beam element that employs nonlinear uniaxial material model (Filippou et al., 1991), a reinforced concrete beam that employs higher order quadrature scheme (Biondini, 2004), fiber-beam models that account for shear and torsion loading (Mohr et al., 2010; Di Re et al., 2016), and more recently, a multiscale beam element that considers three-dimensional constitutive models of steel and concrete (Moyeda and Fish, 2017).

Beam elements specific for prestressed concrete have been developed as well. Aalami (2000) coupled the prestressing steel to the beam element using the tendon as a load resisting element, which enables it to capture the prestressing losses. Ayoub and Filippou (2010) used a fiber-beam element to model pretension concrete elements. Ayoub (2011) extended the formulation to post-tension beams by using a link element between the fiber-beam and tendon elements, but the shear stresses and prestress losses were not considered in the formulation.

The multiscale beam element for analysis of prestressed concrete proposed herein maintains the simplicity characteristic to three-dimensional beam elements, while providing comparable accuracy of three-dimensional nonlinear continuum elements. The proposed multiscale beam element accurately predicts the creep and shrinkage strains, accounts for tendon losses and variable eccentricity, and captures both the shear and bending failures, all in the computational efficient manner. To ensure simulation results are insensitive to the beam element size, a unique constitutive law rescaling procedure that substantially differs from rescaling employed for continuum elements (Bazant and Pijaudier-Cabot, 1989; Oliver, 1989; Liu et al., 2014) is also developed.

The outline of the article is as follows. Section 2 presents the theoretical underpinnings of the multiscale beam element. Details and special considerations for the multiscale prestressed beam element are given in Section 3. A constitutive law recalling procedure for the beam element is presented in Section 4. Numerical validation studies against experimental data are conducted in Section 5. Conclusion and future research efforts are summarized in Section 6.

2. MULTISCALE BEAM ELEMENT FORMULATION

A classical $O(1)$ homogenization theory (Mori and Tanaka, 1973) is not sufficient for multiscale beam height, and therefore, the classical assumption that the coarse-scale strain is constant throughout the representative volume elements (RVE) domain is no longer valid. A modification of the classical $O(1)$ homogenization theory for a prestressed concrete beam of finite height is presented in this section.

2.1 Prestressed Concrete Multiscale Beam Element

The governing equations are stated at the scale of microconstituents, the reinforcing steel, prestressing steel and concrete (Fish et al., 2012; Fish, 2014):

$$\sigma_{ij,j}^{\zeta}(\mathbf{x}) + b_i^{\zeta}(\mathbf{x}) = 0 \quad \text{on} \quad \Omega^{\zeta} \quad (1)$$

$$\sigma_{ij}^{\zeta}(\mathbf{x}) = L_{ijkl}^{\zeta}(\mathbf{x}) \left(\varepsilon_{kl}^{\zeta}(\mathbf{x}) - \mu_{kl}^{\zeta}(\mathbf{x}) \right) \quad \text{on} \quad \Omega^{\zeta} \quad (2)$$

$$\varepsilon_{ij}^{\zeta}(\mathbf{x}) = u_{(i,j)}^{\zeta}(\mathbf{x}) \equiv \frac{1}{2} \left(u_{i,j}^{\zeta} + u_{j,i}^{\zeta} \right) \quad \text{on} \quad \Omega^{\zeta} \quad (3)$$

$$u_i^{\zeta}(\mathbf{x}) = \bar{u}_i^{\zeta}(\mathbf{x}) \quad \text{on} \quad \partial\Omega^{u^{\zeta}} \quad (4)$$

$$\sigma_{ij}^{\zeta}(\mathbf{x}) n_j^{\zeta}(\mathbf{x}) = \bar{t}_i^{\zeta}(\mathbf{x}) \quad \text{on} \quad \partial\Omega^{t^{\zeta}} \quad (5)$$

Throughout this article, it is assumed that microconstituents are homogeneous. The superscript ζ denotes existence of fine-scale features. u_i^{ζ} denotes the displacements; ε_{ij}^{ζ} the total strain; σ_{ij}^{ζ} the Cauchy stress; μ_{ij}^{ζ} the inelastic deformation eigenstrain; and L_{ijkl}^{ζ} the linear elastic fourth-order constitutive tensor that follows Hooke's law. $\partial\Omega^{u^{\zeta}}$ and $\partial\Omega^{t^{\zeta}}$ denote essential and natural boundaries, such that $\partial\Omega^{\zeta} = \partial\Omega^{u^{\zeta}} \cup \partial\Omega^{t^{\zeta}}$ and $\partial\Omega^{u^{\zeta}} \cap \partial\Omega^{t^{\zeta}} = \emptyset$. Spatial derivatives are denoted with a comma; symmetric derivatives are represented by brackets around the subscripts; and Einstein summation convention over repeated indices is employed.

Following Fish and Kuznetsov (2010) and Oskay and Fish (2007), the beam displacements and strains are additively decomposed into the coarse-scale displacement and the fine-scale perturbation

$$u_i^{\zeta} = u_i^c + u_i^1 \quad (6)$$

$$\varepsilon_{ij}^{\zeta} = \varepsilon_{ij}^c + \varepsilon_{ij}^1 \quad (7)$$

where the superscripts c and 1 denote the coarse-scale field and fine-scale perturbation, respectively.

Similarly to Eqs. (6) and (7), the total eigenstrain μ_{ij}^{ζ} can be additively decomposed into mechanical $_{mech}\mu_{ij}$ and initial $_{0}\mu_{ij}$ eigenstrains, the latter describing the initial effects of prestressing, creep, shrinkage, and/or temperature

$$\mu_{ij}^{\zeta} = _{mech}\mu_{ij} + _{0}\mu_{ij} \quad (8)$$

Following Fish (2014) and Fish et al. (2012) and the decomposition of μ_{ij}^ξ in Eq. (8), the perturbation u_i^1 and its corresponding strain tensor ε_{ij}^1 are given by:

$$u_i^1 = H_i^{mn} \varepsilon_{mn}^c + \sum_{\Phi=1}^{\tilde{M}} \tilde{h}_i^{mn(\Phi)} \left({}_{mech} \mu_{mn}^{(\Phi)} + {}_0 \mu_{mn}^{(\Phi)} \right) \quad (9)$$

$$\varepsilon_{ij}^1 = H_{(i,j)}^{mn} \varepsilon_{mn}^c + \sum_{\Phi=1}^{\tilde{M}} P_{ij}^{mn(\Phi)} \left({}_{mech} \mu_{mn}^{(\Phi)} + {}_0 \mu_{mn}^{(\Phi)} \right) \quad (10)$$

$\mu^{(\Phi)}$ represents the coefficients of piecewise approximation of the eigenstrain (Oskay and Fish, 2007)

$$\mu_{ij}^\xi = \sum_{\Phi=1}^{\tilde{M}} \tilde{N}^{(\Phi)} \mu_{ij}^{(\Phi)} \quad (11)$$

$$\tilde{N}^{(\Phi)}(\mathbf{x}) = \begin{cases} 1 & \mathbf{x} \in \Theta^\Phi \\ 0 & \mathbf{x} \notin \Theta^\Phi \end{cases} \quad (12)$$

where \tilde{M} is the number of RVE partitions and $\tilde{N}^{(\Phi)}$ are the eigenstrain piecewise-constant shape functions. Figure 1 depicts the RVE partitions with each partition represented by a different color. Note that over each partition eigenstrains are assumed to be constant.

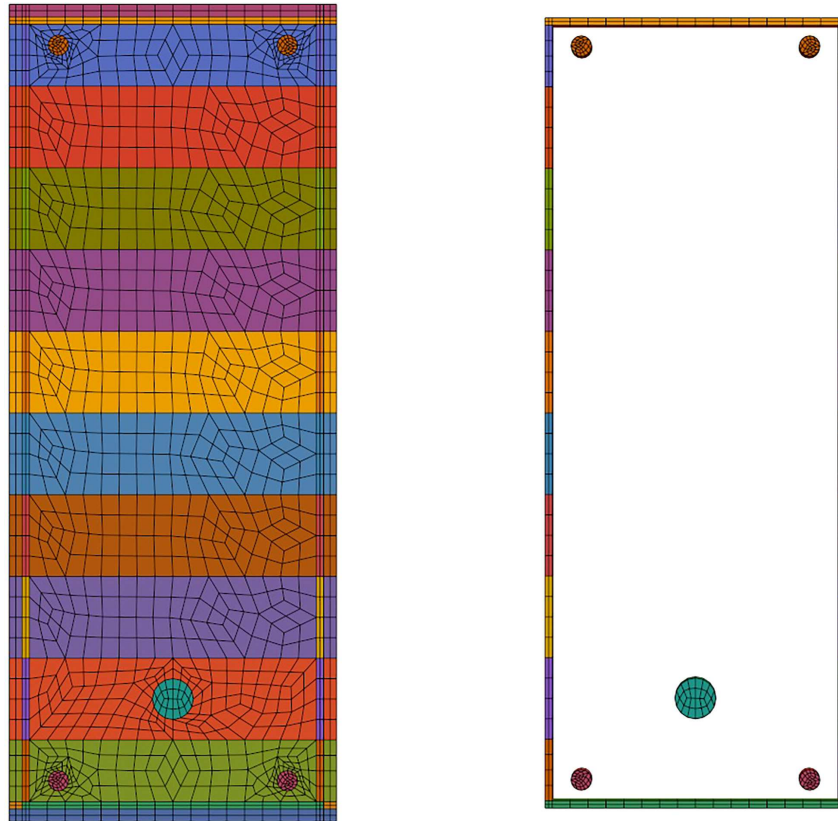


FIG. 1: Unit cell showing partitions

For the analysis of concrete, RVEs can be two-dimensional (2D) when no stirrups are present, or three-dimensional (3D) when stirrups are present or having some periodical feature, such as castellated beams. In the present article, we focus on two-dimensional RVEs with effective representation of stirrups using smearing procedure developed in (Moyeda and Fish, 2017).

Following Fish (2014) and Fish et al. (2012), various influence functions, H_k^{mn} , $\tilde{h}_k^{mn(\Phi)}$, $P_{kl}^{mn(\Phi)}$ are computed by solving the following linear problems on the RVE domain Θ :

$$\left[L_{ijkl} \left(H_{(k,l)}^{mn} + I_{klmn} \right) \right]_{,j} = 0 \quad \text{on } \Theta \quad (13)$$

$$\int_{\partial\Theta_j} H_k^{mn} (\partial\Theta_j) d\gamma = 0 \quad (14)$$

$$\left\{ L_{ijkl} \left[P_{kl}^{mn(\Phi)} - I_{klmn}^{(\Phi)} \right] \right\}_{,j} = 0 \quad \text{on } \Theta \quad (15)$$

$$P_{kl}^{mn(\Phi)} \equiv \tilde{h}_{(k,l)}^{mn(\Phi)} \quad (16)$$

$$\int_{\partial\Theta_j} \tilde{h}_k^{mn(\Phi)} (\partial\Theta_j) d\gamma = 0 \quad (17)$$

$$I_{klmn}^{(\Phi)} = I_{klmn} \tilde{N}^{(\Phi)} \quad (18)$$

where I_{klmn} is the fourth-order symmetric identity tensor and $\partial\Theta_j$ is the boundary of the RVE.

Inserting Eq. (10) into Eq. (7), the total strain ε^z can be written as:

$$\varepsilon_{kl}^z = E_{kl}^{mn} \varepsilon_{mn}^c + \sum_{\Phi=1}^{\tilde{M}} P_{kl}^{mn(\Phi)} {}_m\mu_{mn}^{(\Phi)} + \sum_{\Phi=1}^{\tilde{M}} P_{kl}^{mn(\Phi)} {}_0\mu_{mn}^{(\Phi)} \quad (19)$$

where the elastic strain influence function E_{kl}^{mn} is defined as:

$$E_{kl}^{mn} = \left(H_{(k,l)}^{mn} + I_{klmn} \right) \quad (20)$$

Inserting Eq. (19) into Eq. (2) and rearranging terms, the stress σ^z is equal to:

$$\sigma_{ij}^z = L_{ijkl} \left(E_{kl}^{mn} \varepsilon_{mn} + \sum_{\Phi=1}^{\tilde{M}} (P_{kl}^{mn} - I_{klmn}) {}_{mech}\mu_{mn}^{\Phi} \right) + L_{ijkl} \sum_{\Phi=1}^{\tilde{M}} (P_{kl}^{mn} - I_{klmn}) {}_0\mu_{mn}^{\Phi} \quad (21)$$

2.2 Coarse-Scale Weak Form Formulation

The coarse-scale weak form is obtained by substituting Eq. (21) into Eq. (1), premultiplying by the coarse-scale test function \mathbf{w} and integrating over the coarse-scale domain, which yields the following matrix form (matrices denoted by bold letters)

$$\int_{\Omega} \mathbf{w}^T \nabla \mathbf{L} \left(\mathbf{E} \varepsilon + \sum_{\Phi=1}^{\tilde{M}} (\mathbf{P} - \mathbf{I}) {}_{mech}\mu^{\Phi} \right) d\Omega + \int_{\Omega} \mathbf{w}^T \nabla \mathbf{L} \sum_{\Phi=1}^{\tilde{M}} (\mathbf{P} - \mathbf{I}) {}_0\mu^{\Phi} d\Omega + \int_{\Omega} \mathbf{w}^T \mathbf{b} d\Omega = 0 \quad (22)$$

Applying Green's theorem to the first term of Eq. (22) and rearranging terms yields

$$\int_{\Omega} \nabla \mathbf{w}^T \mathbf{L} \left(\mathbf{E} \varepsilon + \sum_{\Phi=1}^{\tilde{M}} (\mathbf{P} - \mathbf{I}) {}_{mech}\mu^{\Phi} \right) d\Omega = \int_{\Gamma_t} \mathbf{w}^T \mathbf{t} d\Gamma + \int_{\Omega} \mathbf{w}^T \mathbf{b} d\Omega + \int_{\Omega} \nabla \mathbf{w}^T \mathbf{L} \sum_{\Phi=1}^{\tilde{M}} (\mathbf{P} - \mathbf{I}) {}_0\mu^{\Phi} d\Omega \quad (23)$$

Note that the last term on the right-hand side of Eq. (23) is independent of the coarse-scale displacements; it gives rise to an additional force term representing the effects of prestressing. See Appendix A for integration over the composite domain when the RVE is not small when compared to the size of the coarse scale element.

The usual Galerkin approximation is employed for the coarse-scale discretization

$$\begin{aligned}\mathbf{w}^c &= \mathbf{N}^c \mathbf{w}^c \\ \mathbf{u}^c &= \mathbf{N}^c \mathbf{d}^c\end{aligned}\quad (24)$$

$$\begin{aligned}\nabla_s \mathbf{w}^c &= \mathbf{B}^c \mathbf{w}^c \\ \nabla_s \mathbf{u}^c &\equiv \boldsymbol{\varepsilon}^c = \mathbf{B}^c \mathbf{w}^c\end{aligned}\quad (25)$$

where ∇_s is symmetric gradient operator; \mathbf{N}^c and \mathbf{B}^c are coarse-scale shape functions and strain-displacement matrices, respectively; \mathbf{d}^c and \mathbf{w}^c are coarse-scale nodal displacements and nodal values of test functions, respectively. The coarse-scale shape functions are given in the Appendix B.

Substituting Eqs. (24) and (25) into Eq. (23) and requiring arbitrariness of test functions yields the following matrix equations:

$$\mathbf{r}^c = \mathbf{f}_{int}^c - \mathbf{f}_{ext}^c = 0 \quad (26)$$

$$\mathbf{f}_{int}^c = \int_{\Omega} \mathbf{B}^{cT} \mathbf{L} \left(\underbrace{\mathbf{E} \boldsymbol{\varepsilon}^c + \sum_{\Phi=1}^{\tilde{M}} (\mathbf{P} - \mathbf{I})_{\text{mech}} \mu^{\Phi}}_{\boldsymbol{\sigma}^c} \right) d\Omega \quad (27)$$

$$\mathbf{f}_{ext}^c = \int_{\Omega} \mathbf{N}^{cT} \mathbf{t} d\Gamma + \int_{\Omega} \mathbf{N}^{cT} \mathbf{b} d\Omega + \int_{\Omega} \mathbf{B}^{cT} \mathbf{L} \sum_{\Phi=1}^{\tilde{M}} (\mathbf{P} - \mathbf{I})_0 \mu^{\Phi} d\Omega \quad (28)$$

Following Eq. (28), the effects of prestressing, creep, shrinkage, and/or temperature on the external force vector are given by

$$f_0 = \int_{\Omega} \mathbf{B}^{cT} \mathbf{L} \sum_{\Phi=1}^{\tilde{M}} (\mathbf{P} - \mathbf{I})_0 \mu^{\Phi} d\Omega \quad (29)$$

In order to efficiently introduce the effect of the initial eigenstrains for nonlinear problems with evolving damage, it is advantageous to express \mathbf{B}^c as an expansion independent of RVE microstructure, which is the focus of the next section.

2.3 Representation of Coarse-Scale Strain

Since the largest dimension of RVE (i.e., the beam height) is not infinitesimal in comparison to the beam span, it is necessary to account for the variation of coarse-scale strain $\boldsymbol{\varepsilon}_{ij}^c$ over the RVE domain by expanding $\boldsymbol{\varepsilon}_{ij}^c$ as:

$$\boldsymbol{\varepsilon}_{ij}^c = \bar{\boldsymbol{\varepsilon}}_{ij} + \partial_{\alpha} \bar{\boldsymbol{\varepsilon}}_{ij} g_{\alpha}(\mathbf{x}) + \partial_{\alpha\beta} \bar{\boldsymbol{\varepsilon}}_{ij} g_{\alpha\beta}(\mathbf{x}) + \partial_{\alpha\beta\gamma} \bar{\boldsymbol{\varepsilon}}_{ij} g_{\alpha\beta\gamma}(\mathbf{x}) + \partial_{\alpha\beta\gamma\delta} \bar{\boldsymbol{\varepsilon}}_{ij} g_{\alpha\beta\gamma\delta}(\mathbf{x}) \quad (30)$$

where $\partial_{\alpha} \bar{\boldsymbol{\varepsilon}}_{ij}$, $\partial_{\alpha\beta} \bar{\boldsymbol{\varepsilon}}_{ij}$, $\partial_{\alpha\beta\gamma} \bar{\boldsymbol{\varepsilon}}_{ij}$, and $\partial_{\alpha\beta\gamma\delta} \bar{\boldsymbol{\varepsilon}}_{ij}$ are defined as

$$\partial_{\alpha} \bar{\boldsymbol{\varepsilon}}_{ij} = \langle \partial_{\alpha} \boldsymbol{\varepsilon}_{ij} \rangle_{\Theta} \quad (31)$$

$$\partial_{\alpha\beta} \bar{\boldsymbol{\varepsilon}}_{ij} = \langle \partial_{\alpha\beta} \boldsymbol{\varepsilon}_{ij} \rangle_{\Theta} \quad (32)$$

$$\partial_{\alpha\beta\gamma} \bar{\boldsymbol{\varepsilon}}_{ij} = \langle \partial_{\alpha\beta\gamma} \boldsymbol{\varepsilon}_{ij} \rangle_{\Theta} \quad (33)$$

$$\partial_{\alpha\beta\gamma\delta} \bar{\boldsymbol{\varepsilon}}_{ij} = \langle \partial_{\alpha\beta\gamma\delta} \boldsymbol{\varepsilon}_{ij} \rangle_{\Theta} \quad (34)$$

In the above, the operators $\partial_\alpha f$, $\partial_{\alpha\beta} f$, $\partial_{\alpha\beta\gamma} f$, and $\partial_{\alpha\beta\gamma\delta} f$ are defined as

$$\partial_\alpha f = \frac{\partial f}{\partial x_\alpha} \quad (35)$$

$$\partial_{\alpha\beta} f = \frac{\partial^2 f}{\partial x_\alpha \partial x_\beta} \quad (36)$$

$$\partial_{\alpha\beta\gamma} f = \frac{\partial^3 f}{\partial x_\alpha \partial x_\beta \partial x_\gamma} \quad (37)$$

$$\partial_{\alpha\beta\gamma\delta} f = \frac{\partial^4 f}{\partial x_\alpha \partial x_\beta \partial x_\gamma \partial x_\delta} \quad (38)$$

where the bracket operator $\langle f \rangle_\Theta$ defines the average over Θ as

$$\langle f \rangle_\Theta \equiv \bar{f} = \frac{1}{|\Theta|} \int_\Theta f(x_1, x_2, x_3) d\Theta \quad (39)$$

The functions $g_\alpha(\mathbf{x})$, $g_{\alpha\beta}(\mathbf{x})$, $g_{\alpha\beta\gamma}(\mathbf{x})$, and $g_{\alpha\beta\gamma\delta}(\mathbf{x})$ depend on the coarse-scale displacement field definition for the beam element, and are summarized in Appendix B.

2.4 Tangent Stiffness Matrix

For multiscale analysis to be efficient, the coarse-scale strain-displacement matrix \mathbf{B}^c , needs to be expanded so that various expansion terms would be independent of RVE coordinates, and thus, could be precomputed prior to nonlinear analysis.

Following Eq. (30), \mathbf{B}^c can be expanded as

$$\mathbf{B}^c = \bar{\mathbf{B}} + \partial_\alpha \bar{\mathbf{B}} g_\alpha(\mathbf{x}) + \partial_{\alpha\beta} \bar{\mathbf{B}} g_{\alpha\beta}(\mathbf{x}) + \partial_{\alpha\beta\gamma} \bar{\mathbf{B}} g_{\alpha\beta\gamma}(\mathbf{x}) + \partial_{\alpha\beta\gamma\delta} \bar{\mathbf{B}} g_{\alpha\beta\gamma\delta}(\mathbf{x}) \quad (40)$$

The functions $g(\mathbf{x})$ are dependent on the displacement field used for the definition of the coarse-scale beam element. The reader is referred to Appendix B for the derivation of the $g(\mathbf{x})$ family of functions for the third-order beam theory (Heyliger and Reddy, 1988; Reddy, 1997) employed in this study.

The coarse-scale tangent stiffness matrix follows from Eqs. (26)–(28)

$$\mathbf{K}^c = \frac{\partial \mathbf{r}^c}{\partial \mathbf{d}^c} = \int_\Omega \mathbf{B}^c \frac{\partial \sigma^\zeta}{\partial \mathbf{d}^c} d\Omega \quad (41)$$

Differentiating Eq. (21) with respect to the nodal displacements \mathbf{d}^c yields

$$\frac{\partial \sigma^\zeta}{\partial \mathbf{d}} = \mathbf{L}^\zeta \mathbf{E} \left(\begin{array}{c} \bar{\mathbf{B}} + \partial_\alpha \bar{\mathbf{B}} g_\alpha(\mathbf{x}) + \partial_{\alpha\beta} \bar{\mathbf{B}} g_{\alpha\beta}(\mathbf{x}) + \\ \partial_{\alpha\beta\gamma} \bar{\mathbf{B}} g_{\alpha\beta\gamma}(\mathbf{x}) + \partial_{\alpha\beta\gamma\delta} \bar{\mathbf{B}} g_{\alpha\beta\gamma\delta}(\mathbf{x}) \end{array} \right) + \mathbf{L}^\zeta \sum_{\Phi=1}^{\tilde{M}} \left(\mathbf{P}^{(\Phi)} - \mathbf{I}^{(\Phi)} \right) \frac{\partial_{mech} \mu^{(\Phi)}}{\partial \varepsilon^c} \frac{\partial \varepsilon^c}{\partial \mathbf{d}} \quad (42)$$

Note that $(\partial_0 \mu^{(\Phi)})/(\partial \varepsilon^c) = 0$ as it is independent of the coarse-scale displacements.

Inserting Eqs. (42) and (40) into Eq. (41), and accounting for the independence of $\bar{\mathbf{B}}$ on the RVE coordinates, the coarse-scale tangent stiffness matrix can be expressed by

$$\mathbf{K}^c = A_b \int_L \left\{ {}^v \bar{\mathbf{B}}_i^T ({}^m \mathbf{L}_{ij}) {}^v \bar{\mathbf{B}}_j + {}^v \bar{\mathbf{B}}_i^T \left(\sum_{\Phi=1}^{\tilde{M}} {}^m \mathbf{A}_{ij}^{(\Phi)} \frac{\partial_m \mu^{(\Phi)}}{\partial \varepsilon^c} \right) {}^v \bar{\mathbf{B}}_j \right\} dx_1 \quad (43)$$

where

$${}^v\bar{\mathbf{B}} = \left\{ \bar{\mathbf{B}} \quad \partial_\alpha \bar{\mathbf{B}}_\alpha \quad \partial_{\alpha\beta} \bar{\mathbf{B}}_{\alpha\beta} \quad \partial_{\alpha\beta\gamma} \bar{\mathbf{B}}_{\alpha\beta\gamma} \quad \partial_{\alpha\beta\gamma\delta} \bar{\mathbf{B}}_{\alpha\beta\gamma\delta} \right\} \quad (44)$$

$${}^m\mathbf{L}_{ij} = \frac{1}{|\Theta|} \int_{\Theta} g_i^v \mathbf{L}^\xi \mathbf{E} g_j^v d\Theta \quad (45)$$

$$g^v = \left\{ 1 \quad g_\alpha(\mathbf{x}) \quad g_{\alpha\beta}(\mathbf{x}) \quad g_{\alpha\beta\gamma}(\mathbf{x}) \quad g_{\alpha\beta\gamma\delta}(\mathbf{x}) \right\} \quad (46)$$

$${}^m\mathbf{A}_{ij}^{(\Phi)} = \frac{1}{|\Theta|} \int_{\Theta} g_i^v \mathbf{L}^\xi \left(\mathbf{P}^{(\Phi)} - \mathbf{I}^{(\Phi)} \right) g_j^v d\Theta \quad (47)$$

The value of $(\partial_m \mu^{(\Phi)})/(\partial \varepsilon^c)$ depends on the constitutive models of microconstituents. One of the salient features of the proposed nonlinear multiscale beam formulation is that a variety of materials models can be utilized depending on the application without modifying the overall framework.

2.5 Force Vector for Initial Eigenstrains

It follows from the weak form described in Section 2.2 that the effects of initial eigenstrains, such as prestressing, temperature, creep, and shrinkage, can be accounted for by introducing a force vector appearing in Eq. (29).

Inserting expansion of \mathbf{B}^c in Eq. (40) into Eq. (29), the initial eigenstrain force vector f_0 is given by

$$f_0 = \int_{\Omega} {}^v\bar{\mathbf{B}}_i^T \sum_{\Phi=1}^{\tilde{M}} {}^v\mathbf{A}_i^{(\Phi)} {}_0\mu^{(\Phi)} d\Omega \quad (48)$$

where

$${}^v\mathbf{A}_i^{(\Phi)} = \frac{1}{|\Theta|} \int_{\Theta} \mathbf{g}_i^v \mathbf{L}^\xi \left(\mathbf{P}^{(\Phi)} - \mathbf{I}^{(\Phi)} \right) d\Theta \quad (49)$$

2.6 Reduced Order Computational RVE Problem

At each Newton iteration of the coarse-scale solver, it is necessary to calculate the strain and eigenstrain in each partition, for each Gauss point of the beam element. This is carried out by solving the reduced system of equations. See Fish (2014) and Oskay and Fish (2007) for details.

Let $\varepsilon_{kl}^{(\Psi)}$ be the partition strain, which is the average of ε_{kl}^ξ in Eq. (19) over partition $\Theta^{(\Psi)}$, defined as

$$\varepsilon_{kl}^{(\Psi)} = E_{kl}^{mn(\Psi)} \varepsilon_{mn}^c + \sum_{\Phi=1}^{\tilde{M}} P_{kl}^{mn(\Psi\Phi)} {}_{mech}\mu_{mn}^{(\Phi)} \quad (50)$$

where

$$E_{kl}^{mn(\Psi)} = \frac{1}{|\Theta^{(\Psi)}|} \int_{\Theta^{(\Psi)}} E_{kl}^{mn} d\Theta \quad (51)$$

$$P_{kl}^{mn(\Psi\Phi)} = \frac{1}{|\Theta^{(\Psi)}|} \int_{\Theta^{(\Psi)}} P_{kl}^{mn(\Phi)} d\Theta \quad (52)$$

Equation (50) is solved using the fine-scale Newton method at the RVE level nested with the coarse-scale Newton method at the beam level. For details see Fish (2014); Oskay and Fish (2007), and Fish et al. (2015).

3. PRESTRESSED BEAM ELEMENT

3.1 Prestressing Tendon Eccentricity

In the prestressed concrete beam, the position of the prestressing steel is changing along the beam so that the action of the prestressing balances out the effect of external load acting on the beam (Lin, 1963). Due to varying position of prestressing, RVEs vary along the beam length. Figure 2 depicts a simply supported beam with a parabolic tendon profile, showing the corresponding RVEs, in meshes consisting of 1, 2, and 4 coarse-scale (beam) elements.

For comparison, the equivalent load for a simply supported beam with a parabolic tendon profile is given by Lin (1963):

$$w_{eq} = \frac{8Py}{S^2} \quad (53)$$

where P is equal to prestress load, S is the beam span, and y is the cable sag at a midpoint measured from a line passing through the cable end points. For a 10 m span beam, the theoretical deflection is 6.98 mm, while the results using two and four multiscale beam elements are 6.99 mm for an error of 0.13%.

3.2 Initial Strain in Prestressed Steel

For the posttension beam, instantaneous losses in the prestressing force (Nilson, 1987) due to frictional forces and anchorage slip, must be taken into account. Positions of RVEs depend on the number of coarse-scale elements (Fig. 2). The prestressing force, less the losses due to friction and anchorage slip, is evaluated at the position of RVEs along the span and the initial strain in the prestressing steel. The initial strain over the steel partitions is used in Eq. (48) to calculate the equivalent loads for the element.

3.3 Consideration of Creep and Shrinkage

Creep and shrinkage has been recognized (Zia, 1979; Bazant, 1998) as an intricate phenomenon in concrete structures. Modern design codes (fib CEB-FIP, 2010), (AASHTO, 2014), provide estimates of creep and shrinkage strains. To account for creep and shrinkage effects in the multiscale beam context, the appropriate strains in various partitions throughout the time history must be considered. The eigenstrains induced due to creep and shrinkage are calculated for every concrete partition, at every construction stage, and subsequently, time-varying equivalent force vector is computed based on Eq. (48) throughout the coarse-scale analysis.

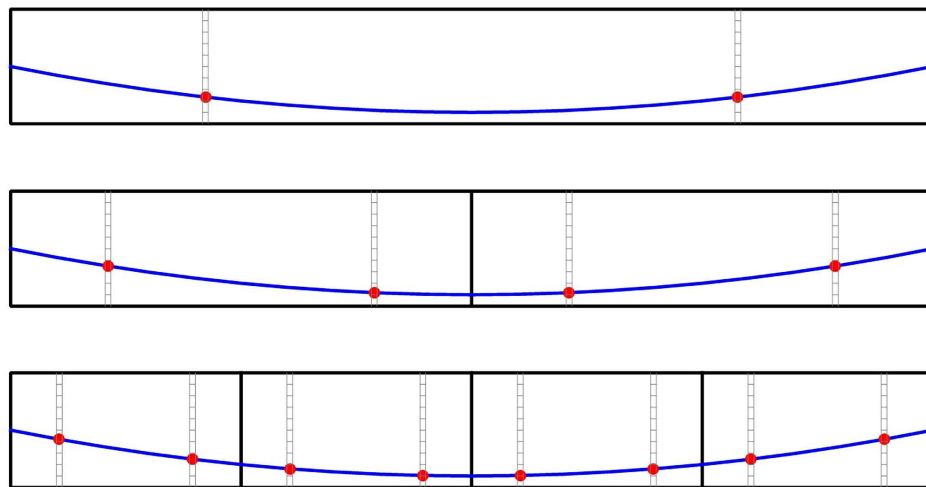


FIG. 2: Position of prestressing steel shown in *circles*, for a parabolic tendon profile in finite element meshes having 1, 2, and 4 beam elements

4. REGULARIZATION OF THE MULTISCALE BEAM FORMULATION

Strain softening resulting from damage is known to give rise to mesh size dependency. Among the well-known regularization techniques that circumvent (at least partially) solution dependence on the mesh size are nonlocal methods, rescaling or smeared crack methods, and viscous regularization methods (Belytschko and Fish, 1988; Bazant and Pijaudier-Cabot, 1989). From a practical point of view, smeared crack or rescaling approaches (Oliver, 1989; Bazant and Pijaudier-Cabot, 1989; Cervera, 2008) are advantageous as they only require rescaling of constitutive equations based on the mesh size. The basic idea of these approaches is as follows: when the blunt crack is formed as a result of element removal (or reduction of stress to nearly zero value without element removal) the energy removed from the mesh divided by the new surface introduced should be invariant to the element size. It is a trivial exercise to show that for this to be true, the area under the effective stress-strain curve has to be rescaled by a factor inversely proportional to the characteristic size of the element. The rescaling by a factor proportional to characteristic element size is a consequence of the fact that the volume of a continuum element removed divided by a new surface introduced is of the order of characteristic element size.

In this section we show that for concrete beams, the rescaling factor should be different than for continuum elements. Consider a beam of span S (Fig. 3) subjected to a constant moment that is sufficiently large to induce cracking. In the computational beam model, cracks are formed at the beam element quadrature points. Thus, a new surface area introduced by cracking is equal to the product of the total number of quadrature points, the crack height, and the beam width. The volume of the concrete (depicted by shaded areas in Fig. 3) where the stress drops to zero (or nearly zero) can be approximated by a product of the distance between the two cracks oriented on the opposite side of the beam, the crack height, and the beam width. Figure 3 depicts the ratio of volume and surface area for the beam discretized into 1, 2, 3, 4, and 5 elements of length L_e .

The beam of two elements is considered, $S = 2L_e$, as the baseline for which the constitutive equations were calibrated to fit experimental data. In case of span to element size ratio different than 2, the material model needs to be rescaled as follows:

$$R = \left(\frac{2L_e}{S} \right)^{-0.64} \quad (54)$$

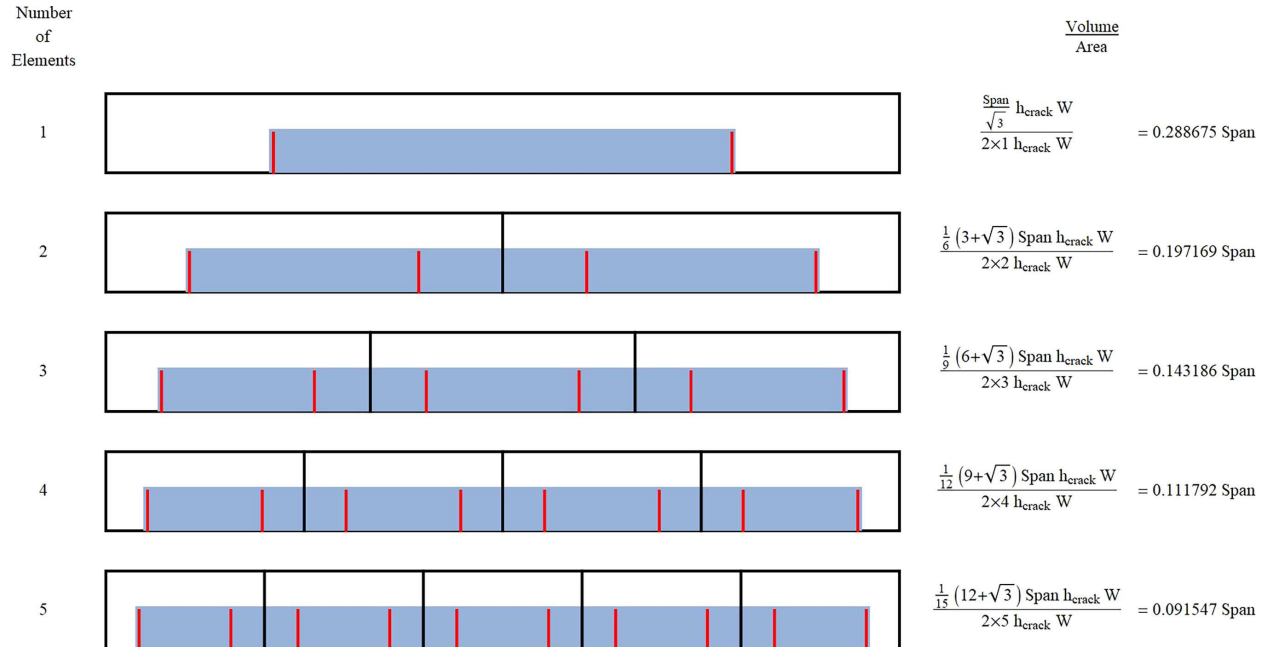


FIG. 3: Ratio of cracked volume to crack surface area for different element lengths

to provide the best fit of the volume to surface area ratios depicted in Fig. 3. In the next section we show that with the rescaling introduced in Eq. (54), the results are nearly independent of the beam element length.

5. MODEL VALIDATION

5.1 Verification of Rescaling Approach

We first study the rescaling approach introduced in Eq. (54) by considering the beam tested by Saqan and Frosch (2009). The beam is simply supported with a span of 4.06 m, a width of 356 mm, and a depth of 711 mm (Fig. 4). The beam is reinforced with four 12.7 mm straight prestressing strands with an ultimate strength of 1862 MPa. The concrete has a compressive strength of 52.1 MPa. For the constitutive modeling of concrete, we assume an isotropic damage model proposed by Pijaudier-Cabot and Mazars (2001) with damage parameters A_t , B_t , A_c , and B_c obtained using the following two-step procedure. We first reconstruct the stress-strain curves (in tension and compression) based on the guidelines suggested in (fib CEB-FIP, 2010) for the specified concrete grade. Second, we employ inverse optimization procedures to identify damage model parameters that provide the best fit to the reconstructed stress-strain curves in step one. For the experimental beam in Saqan and Frosch (2009), the following material parameters were used: modulus of elasticity = 30,411 MPa, Poisson's ratio = 0.2, $A_t = 2.0$, $B_t = 21,000$, $A_c = 1.6$, and $B_c = 1600$.

For the finite element model, we consider two, four and six beam elements, and the material model is rescaled by Eq. (54). The 30 mm displacement at a midspan is applied in 100 steps, and the results are shown in Fig. 5. It

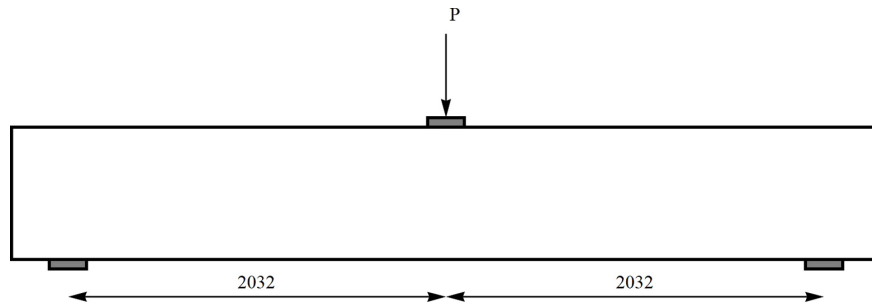


FIG. 4: Beam test setup for simply supported rectangular beam

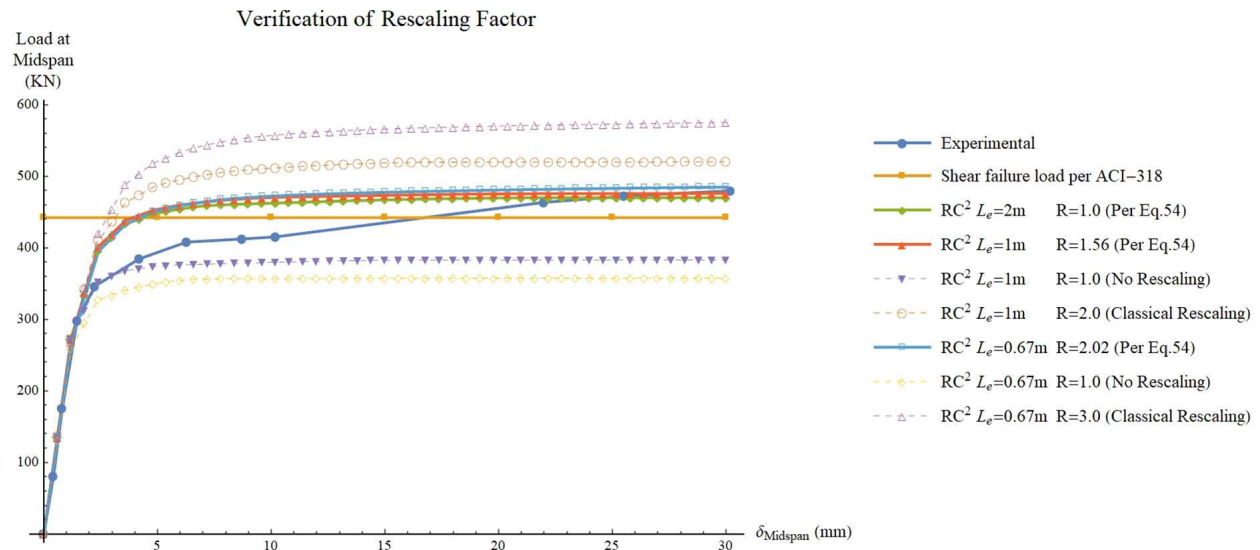


FIG. 5: Mesh sensitivity studies and comparison to ACI-318 code and experimental results

can be seen that without rescaling or with the classical rescaling proportional to the characteristic element size, the results are highly sensitive to the mesh size. With the proposed rescaling, practically no mesh sensitivity is observed and the numerical simulations results (tagged as RC²) are in good agreement with the experimental results. Figure 5 also depicts the failure load based on the ACI-318 code (ACI, 2014), which shows a reasonable agreement with the experimental results.

5.2 Shear Test on TxDOT Type A Beam

We consider a simply supported I beam, a cross section known as the Texas Department of Transportation (TxDOT) A beam, tested at the University of Houston (Laskar et al., 2010). The beam is simply supported with a span of 7.32 m and a depth of 713 mm (Fig. 6). The beam is reinforced with twelve 12.7 mm straight prestressing strands with an ultimate strength of 1862 MPa. The beam is reinforced with four No. 5 rebars on the top and stirrups No. 2 at with 0.25 m spacing. The reinforcing steel has a yield strength of 410 MPa and the concrete has a strength of 71 MPa. The concrete is modeled using isotropic damage model (Pijaudier-Cabot and Mazars, 2001) with the following material parameters: modulus of elasticity = 41,700 MPa, Poisson's ratio = 0.2, $A_t = 1.5$, $B_t = 21,000$, $A_c = 1.9$, and $B_c = 1500$.

The analysis was performed using four coarse-scale elements with the interior nodes located under loads and at a midspan. The prescribed displacement of 35 mm was applied over 50 load increments at the points of load application. The multiscale (RC²) simulation was compared in Fig. 7 with the experimental results (Laskar et al., 2010) and the ACI-318 code (ACI, 2014). It can be seen that the multiscale beam accurately predicts the failure load and the overall behavior of the beam, whereas the ACI-318 underestimates the capacity by more than 25%.

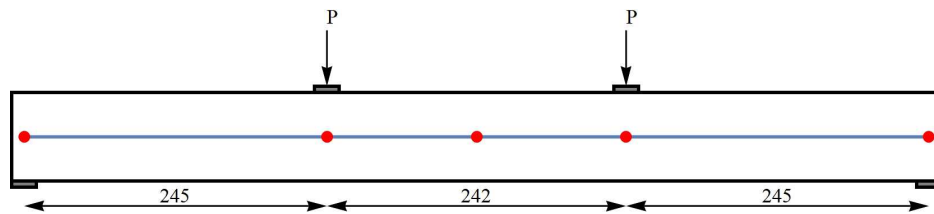


FIG. 6: Experimental setup and finite element model for the TxDOT A beam. Beam elements are shown in the center of the beam

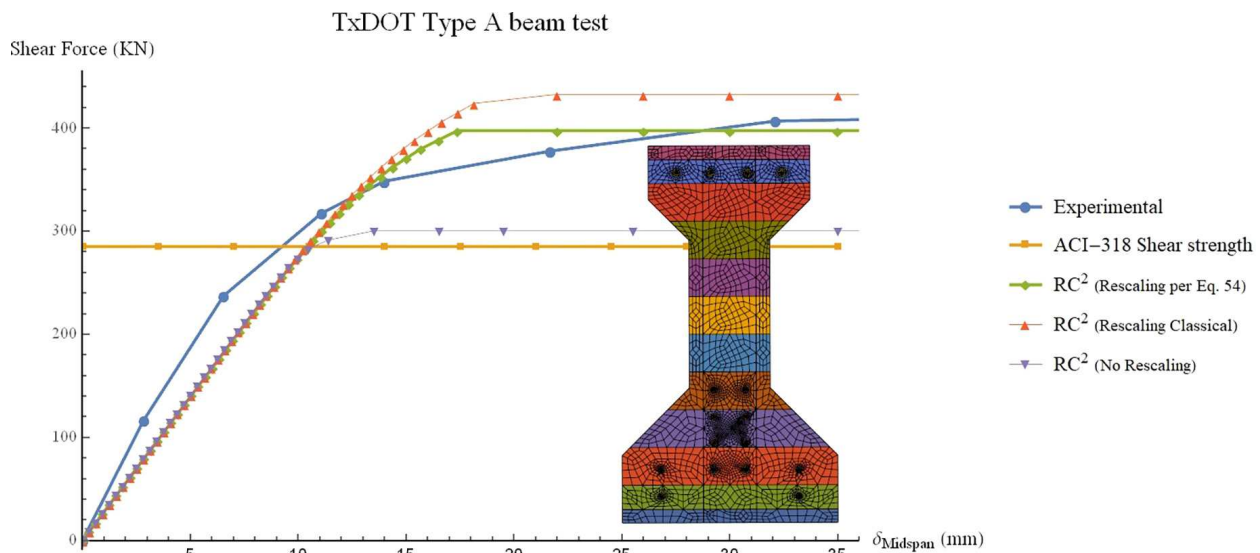


FIG. 7: TxDOT Type A beam. Comparison of RC2, ACI-318 code and experimental results. Simulation results with no rescaling and with classical rescaling are also shown

5.3 Continuous Posttensioned Beam

A continuous posttensioned beam was tested at the RWTH Aachen University (Herbrand et al., 2018). The beam has a rectangular cross section of a depth of 800 mm and a width of 250 mm. The beam has two tendons with a parabolic profile (Fig. 8). Each prestressing tendon is made up of three 0.6" strands with an ultimate load of 1950 MPa. The beam is reinforced with six rebars 25 mm in diameter at the top and bottom; stirrups are 10 mm in diameter spaced at 0.25 m; the yield stress for the rebars is 557 MPa for the longitudinal rebars, and 520 for the stirrups. The concrete has a strength of 51 MPa with constitutive model based on the isotropic damage model (Pijaudier-Cabot and Mazars, 2001) with the following material parameters: modulus of elasticity = 25,824 MPa, Poisson's ratio = 0.2, $A_t = 1.1$, $B_t = 15,000$, $A_c = 2.2$, and $B_c = 1500$. The experimental setup is shown in Fig. 8.

The analysis was performed using four coarse-scale elements, a displacement under the loads was applied in 100 steps. Figure 9 depicts the load-deflection curves obtained by the multiscale beam formulation and the ACI-318 code, both of which are in good agreement with the experimental results.

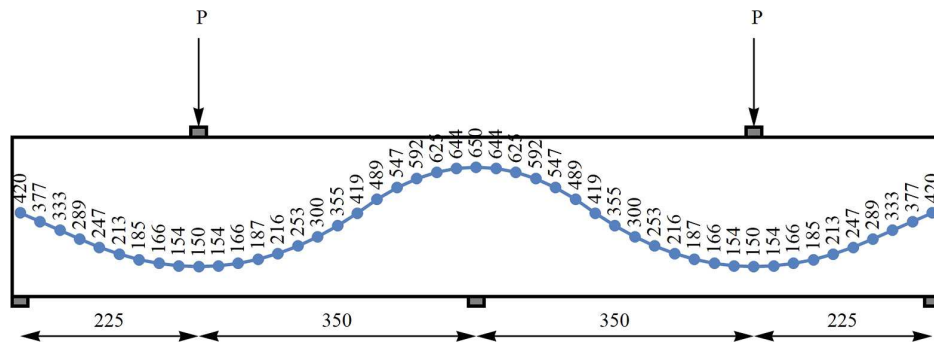


FIG. 8: Experimental setup for continuous posttensioned beam

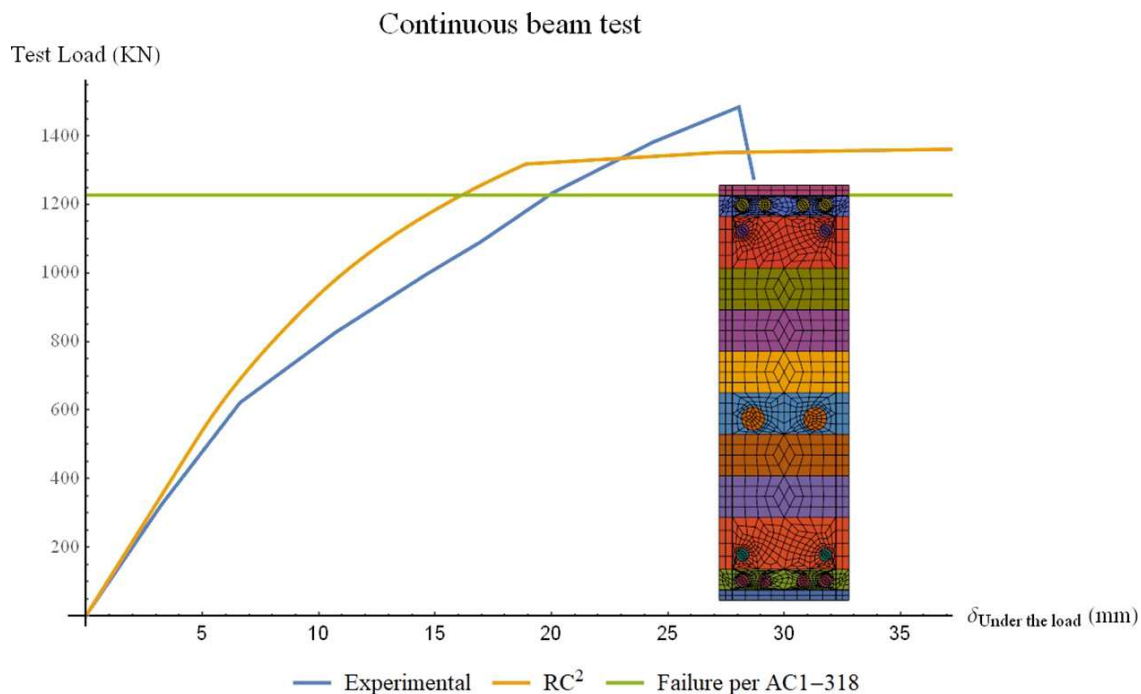


FIG. 9: Continuous posttensioned beam. Comparison of RC^2 , ACI-318 code, and experimental results

6. CONCLUSIONS

A multiscale prestressed beam element for the analysis of prestressed concrete was developed. The multiscale beam element is capable of capturing flexural, shear, and torsion modes of failure. Prestressing tendons with variable eccentricity are accommodated by the formulation, and effects due to creep and shrinkage are considered. In terms of computational cost, the multiscale beam has a fraction of degrees-of-freedom in comparison to the full 3D solid modeling at the scale of reinforcement. It is instructive to point out that the failure load predicted by the multiscale beam element and that recommended by the ACI-318 code are in good agreement for a rectangular beam cross-section. However, for non-rectangular cross-sections, the failure load predicted by the ACI-318 code is shown to be inaccurate. This confirms the observations made in Herbrand et al. (2018).

Finally, a simple rescaling methodology for the multiscale beam element, which differs from the classical rescaling approach for continuum elements, is developed and renders simulation results nearly mesh size insensitive.

Future research efforts will focus on the development of multiscale shell element for reinforced and prestressed concrete, consideration of bond-slip effects between the concrete and rebar, and three phase formulation, where the concrete is considered as a two-scale material.

REFERENCES

- Aalami, B.O., Structural Modeling of Posttensioned Members, *J. Struct. Eng.*, vol. **126**, no. 2, pp. 157–162, 2000.
- American Association of State Highway and Transportation Officials, *AASHTO LRFD Bridge Design Specifications*, Washington DC: AASHTO, 2014.
- ACI Committee, *Building Code Requirements for Structural Concrete ACI-318*, Farmington Hills, MI: American Concrete Institute, 2014.
- Ayoub, A. and Filippou, F.C., Finite-Element Model for Pretensioned Prestressed Concrete Girders, *J. Struct. Eng.*, vol. **136**, no. 4, pp. 401–409, 2010.
- Ayoub, A., Nonlinear Finite-Element Analysis of Posttensioned Concrete Bridge Girders, *J. Bridge Eng.*, vol. **16**, no. 3, pp. 479–489, 2011.
- Bazant, Z., Caner, F., Carol, I., Adley, M., and Akers, S., Microplane Model M4 for Concrete. Part I: Formulation with Work-Conjugate Deviatoric Stress, *J. Eng. Mech. ASCE*, vol. **126**, no. 9, pp. 944–953, 2000.
- Bazant, Z.P. and Pijaudier-Cabot, G., Measurement of Characteristic Length of Nonlocal Continuum, *J. Eng. Mech.*, vol. **115**, no. 4, pp. 755–767, 1989.
- Bazant Z.P., Material Models for Structural Creep Analysis, in *Mathematical Modeling of Creep and Shrinkage of Concrete*, Z.P. Bazant, Ed., New York, NY: John Wiley & Sons Ltd., pp. 99–215, 1998.
- Belytschko, T., Fish, J., and Engelmann, B., A Finite Element with Embedded Localization Zones, *Comput. Methods Appl. Mech. Eng.*, vol. **70**, pp. 59–89, 1988.
- Biondini, F., A Three-Dimensional Finite Beam Element for Multiscale Damage Measure and Seismic Analysis of Concrete Structures, *13th World Conf. Earthquake Eng.*, Vancouver, B.C. Canada, paper no. 2963, 2004.
- Cervenka, J. and Cervenka, V., Three Dimensional Combined Fracture-Plastic Material Model for Concrete Including Creep and Rate Effect for Dynamic Loading, *Int. J. Plasticity*, vol. **24**, no. 12, pp. 2192–2220, 2008.
- Cervera, M., A Smeared-Embedded Mesh-Corrected Damage Model for Tensile Cracking, *Int. J. Numer. Meth. Eng.*, vol. **76**, pp. 1930–1954, 2008.
- Di Re, P., Addessi, D., and Filippou, F., 3D Beam-Column Finite Element under Non-Uniform Shear Stress Distribution due to Shear and Torsion, *ECCOMAS Congress 2016, VII European Cong. Comput. Methods Appl. Sci. Eng.*, Crete Island, Greece, 2016.
- Filippou, F.C., Spacone, E., and Taucer, F.F., A Fiber Beam-Column Element for Seismic Response Analysis of Reinforced Concrete Structures, Earthquake Engineering Research Center, College of Engineering, University of California, Berkeley, Rep. UCB/EERC-91/17, 1991.
- Fish, J., *Practical Multiscale*, New York: John Wiley & Sons, 2014.

- Fish, J., Filonova, V., and Fafalis, D., Computational Continua Revisited, *Int. J. Numer. Meth. Eng.*, vol. **102**, pp. 332–378, 2015.
- Fish, J., Filonova, V., and Yuan, Z., Reduced Order Computational Continua, *Comput. Methods Appl. Mech. Eng.*, vol. **221–222**, pp. 104–116, 2012.
- Fish, J. and Kuznetsov, S., Computational Continua, *Int. J. Numer. Methods Eng.*, vol. **84**, pp. 774–802, 2010.
- Grassl, P., Xenos, D., Nystrom, U., Rempling, R., and Gylltoft, K., CDPM2: A Damage-Plasticity Approach to Modelling the Failure of Concrete, *Int. J. Solids and Struct.*, vol. **50**, no. 24, pp. 3805–3816, 2013.
- Herbrand, M., Kueres, D., Classen, M., and Hegger, J., Experimental Investigations on the Shear Capacity of Prestressed Concrete Continuous Beams with Rectangular and I-Shaped Cross-Sections, *High Tech Concrete: Where Technology and Engineering Meet, Proc. 2017 fib Symp.*, Maastricht, The Netherlands: Springer International Publishing, 2018.
- Heyliger, P. and Reddy, J.N., A Higher Order Beam Finite Element for Bending and Vibration Problems, *J. Sound Vibrat.*, vol. **126**, no. 2, pp. 309–326, 1988.
- International Federation for Structural Concrete, *fib Model Code for Concrete Structures 2010*, Lausanne Switzerland: International Federation for Structural Concrete, 2010.
- Laskar, A., Hsu, T., and Mo, Y.L., Shear Strengths of Prestressed Concrete Beams Part 1: Experiments and Design, *ACI Struct. J.*, vol. **107**, no. 3, pp. 330–339, 2010.
- Lee, J. and Fenves, G.L., Plastic-Damage Model for Cyclic Loading, *J. Eng. Mech.*, vol. **124**, no. 8, pp. 892–900, 1998.
- Lin, T.Y., Load-Balancing Methods for Design and Analysis of Prestressed Concrete, *J. Am. Concrete Inst.*, vol. **60**, no. 6, pp. 719–742, 1963.
- Liu, Y., Filonova, V., Hu, N., Yuan, Z., Fish, J., Yuan, Z., and Belytschko, T., A Regularized Phenomenological Multiscale Damage Model, *Int. J. Numer. Methods Eng.*, vol. **99**, pp. 867–887, 2014.
- Mohr, S., Bairán, J., and Marí, A., A Frame Element Model for the Analysis of Reinforced Concrete Structures under Shear and Bending, *Eng. Struct.*, vol. **32**, pp. 3936–3956, 2010.
- Mori, T. and Tanaka, K., Average Stress in Matrix and Average Elastic Energy of Materials with Misfitting Inclusions, *Acta Metallurgica*, vol. **21**, 1973.
- Moyeda, A. and Fish, J., Towards Practical Multiscale Approach for Analysis of Reinforced Concrete Structures, *J. Comput. Mech.*, 2017. DOI: 10.1007/s00466-017-1521-1
- Nilson, A.H., *Design of Prestressed Concrete*, New York: John Wiley & Sons, Inc., 1987.
- Oliver, J., A Consistent Characteristic Length for Smeared Cracking Models, *Int. J. Numer. Methods Eng.*, vol. **28**, pp. 461–474, 1989.
- Oskay, C. and Fish, J., Eigendefor-mation-based Reduced Order Homogenization for Failure Analysis of Heterogeneous Materials, *Comput. Methods Appl. Mech. Eng.*, vol. **196**, no. 7, pp. 1216–1243, 2007.
- Pijaudier-Cabot, G. and Mazars, J., Damage Models for Concrete, in *Handbook of Materials Behavior Models*, J. LeMaitre, Ed., San Diego, CA: Academic Press, pp. 500–512, 2001.
- Reddy, J.N., On Locking-Free Shear Deformable Beam Finite Elements, *Comput. Meth. Appl. Mech. Eng.*, vol. **149**, pp. 113–132, 1997.
- Saqan, E. and Frosch, R., Influence of Flexural Reinforcement on Shear Strength of Prestressed Concrete Beams, *ACI Struct. J.*, vol. **106**, no. 1, pp. 60–68, 2009.
- Willam, K.J. and Warnke, E.P., Constitutive Model for the Triaxial Behavior of Concrete, *IABSE Reports on the Working Commissions*, Zurich, Switzerland: International Association of Bridge and Structural Engineering, 1974.
- Zia, P., Preston, H.K., Scott, N.L., and Workman, E.B., Estimating Prestress Losses, *Concrete Int.*, vol. **6**, pp. 32–38, 1979.

APPENDIX A. NONLOCAL QUADRATURE

If the RVE is not infinitesimally small in the direction of the axis, when compared to the coarse scale element length, which would be the case when an irregular pattern of stirrups is to be analyzed, classical homogenization that assumes a constant strain through the RVE is not appropriate, the method of reduced order of computational continua RC² (Fish and Kuznetsov, 2010; Fish et al., 2012, 2015) solves the problem of scale separation.

The RVE's used for the analysis of prestressed beams have a finite size equal to the beam depth and width, and it is infinitesimal small in the axial direction.

In case of an infinitesimal RVE domain, the classical two-scale integration scheme given by

$$\lim_{\zeta^\alpha \rightarrow 0} \int_{\Omega_X^\zeta} f^\zeta(\mathbf{X}, \mathbf{Y}) d\Omega = \lim_{\zeta^\alpha \rightarrow 0} + \sum_{i=1}^N \int_{\Theta_Y} \frac{1}{|\Theta_Y|} J^e(x_I) W_I f^\zeta(x_I, \mathbf{Y}) d\Theta \quad (\text{A.1})$$

In Eq. (A.1) the gauss points coincide with classical gauss quadrature points.

When one or more dimensions are comparable to the size of the coarse scale element, Eq. (A.1) has to be replaced by the nonlocal quadrature scheme, positions of the integration points and their weights are a function of the RVE size, and follow (Fish and Kuznetsov, 2010; Fish, 2014; Fish et al., 2015):

$$\int_{\Omega_X^\zeta} f(\mathbf{X}) d\Omega = \sum_{i=1}^{\hat{N}} \int_{\Theta_{\hat{x}_I}} \frac{1}{|\Theta_{\hat{x}_I}|} J^e(\hat{x}_I, \chi) \hat{W}_I f^\zeta(\hat{x}_I, \chi) d\Theta \quad (\text{A.2})$$

where the positions of the nonlocal quadrature points are expressed as \hat{x}_I , the weights \hat{W}_I and J^e is the Jacobian of the coarse scale element. Table A.1 list the position of the non-local quadrature points and their weights as a function of the RVE expressed as $\Theta' = \Theta/J^e$ (Fish, 2014; Fish and Kuznetsov, 2010).

APPENDIX B. COARSE-SCALE DISPLACEMENT FIELD

The higher order beam theory presented by Heyliger and Reddy (1988) and Reddy (1997) has 18 degrees of freedom (dof's), eight dof's in each end node and two additional dof's in the middle node that can be condensed out from the solution; such that the displacements are expressed as:

$$\begin{Bmatrix} {}^c u_1 \\ {}^c u_2 \\ {}^c u_3 \end{Bmatrix} = \mathbf{N}^c \left\{ \begin{matrix} {}^c u_1^1 & {}^c u_2^1 & {}^c u_3^1 & \theta_1^1 & \theta_2^1 & \theta_3^1 & \gamma_2^1 & \gamma_3^1 & {}^c u_1^2 & {}^c u_2^2 & {}^c u_3^2 & \theta_1^2 & \theta_2^2 & \theta_3^2 & \gamma_2^2 & \gamma_3^2 & \gamma_2^3 & \gamma_3^3 \end{matrix} \right\}^T \quad (\text{B.1})$$

where ${}^c u_i$ denotes the three-dimensional displacements; ${}^c u_i$ the displacement at the centerline of the beam in direction x_1 ; and θ_1 the rotation around the x_1 ; $\theta_2 = (\partial {}^c u_3^0)/(\partial x_1)$ and $\theta_3 = (\partial {}^c u_2^0)/(\partial x_1)$. γ_2 and γ_3 are the cross-sectional rotations around the x_2 and x_3 , respectively.

The shape functions used to describe the displacement field in Eq. (B.1) are:

TABLE A.1: Positions and Weights of Nonlocal Quadrature Points

Number of Gauss Points	Positions of the nonlocal gauss points (ξ_I)	Nonlocal weights (\hat{W}_I)
2-Point rule	$\xi_{1,2} = \pm \sqrt{\frac{1}{3} - \frac{\Theta'^2}{12}}$	$\hat{W}_{1,2} = 1$
3-Point rule	$\xi_{1,3} = \pm \frac{\sqrt{60 - 35\Theta'^2}}{10}$ $\xi_2 = 0$	$\hat{W}_{1,3} = \frac{5(4 - \Theta'^2)}{3(12 - 7\Theta'^2)}$ $\hat{W}_2 = 2 - 2\hat{W}_1$

$$\mathbf{N}^c = \begin{bmatrix}
1 - x_1/L & 0 & 0 \\
\frac{6(L - x_1)x_1x_2}{L^3} & \frac{(L - x_1)^2(L + 2x_1)}{L^3} & 0 \\
\frac{6(L - x_1)x_1x_3}{L^3} & 0 & \frac{(L - x_1)^2(L + 2x_1)}{L^3} \\
0 & \left(-1 + \frac{x_1}{L}\right)x_3 & \frac{(L - x_1)x_2}{L} \\
\frac{(L - 3x_1)(L - x_1)x_3}{L^2} & 0 & -\frac{(L - x_1)^2x_1}{L^2} \\
-\frac{(L - 3x_1)(L - x_1)x_2}{L^2} & \frac{(L - x_1)^2x_1}{L^2} & 0 \\
\frac{(L - 2x_1)(L - x_1)x_3\left(1 - \frac{4x_3^2}{3h^2}\right)}{L^2} & 0 & 0 \\
\frac{(L - 2x_1)(L - x_1)x_2\left(1 - \frac{4x_2^2}{3b^2}\right)}{L^2} & 0 & 0 \\
x_1/L & 0 & 0 \\
\frac{6x_1(-L + x_1)x_2}{L^3} & \frac{(3L - 2x_1)x_1^2}{L^3} & 0 \\
\frac{6x_1(-L + x_1)x_3}{L^3} & 0 & \frac{(3L - 2x_1)x_1^2}{L^3} \\
0 & -\frac{x_1x_3}{L} & \frac{x_1x_2}{L} \\
\frac{x_1(-2L + 3x_1)x_3}{L^2} & 0 & \frac{(L - x_1)x_1^2}{L^2} \\
\frac{(2L - 3x_1)x_1x_2}{L^2} & \frac{x_1^2(-L + x_1)}{L^2} & 0 \\
-\frac{(L - 2x_1)x_1x_3\left(1 - \frac{4x_3^2}{3h^2}\right)}{L^2} & 0 & 0 \\
-\frac{(L - 2x_1)x_1x_2\left(1 - \frac{4x_2^2}{3b^2}\right)}{L^2} & 0 & 0 \\
\frac{4(L - x_1)x_1x_3\left(1 - \frac{4x_3^2}{3h^2}\right)}{L^2} & 0 & 0 \\
\frac{4(L - x_1)x_1x_2\left(1 - \frac{4x_2^2}{3b^2}\right)}{L^2} & 0 & 0
\end{bmatrix}^T \quad (\text{B.2})$$

The family of $g(\mathbf{x})$ functions corresponding to the Heyliger and Reddy (1988) and Reddy (1997) beam formulation are obtained by substituting the known values in Eq. (40) and solving for the $g(\mathbf{x})$ functions, which yields

$$g_1 = 0 \quad (\text{B.3})$$

$$g_2 = x_2 \quad (\text{B.4})$$

$$g_3 = x_3 \quad (\text{B.5})$$

$$g_{11} = 0 \quad (\text{B.6})$$

$$g_{12} = x_1 x_2 \quad (\text{B.7})$$

$$g_{13} = x_1 x_3 \quad (\text{B.8})$$

$$g_{22} = -\frac{h_2^2}{24} + \frac{x_2^2}{2} \quad (\text{B.9})$$

$$g_{33} = -\frac{h_3^2}{24} + \frac{x_3^2}{2} \quad (\text{B.10})$$

$$g_{122} = -\frac{1}{8} x_1 (h_2^2 - 4x_2^2) \quad (\text{B.11})$$

$$g_{133} = -\frac{1}{8} x_1 (h_3^2 - 4x_3^2) \quad (\text{B.12})$$

$$g_{222} = -\frac{1}{24} x_2 (h_2^2 - 4x_2^2) \quad (\text{B.13})$$

$$g_{333} = -\frac{1}{24} x_3 (h_3^2 - 4x_3^2) \quad (\text{B.14})$$

$$g_{1122} = \frac{1}{192} (h_2^2 - 4x_2^2) (|\Theta|_1^2 - 12x_1^2) \quad (\text{B.15})$$

$$g_{1133} = \frac{1}{192} (h_3^2 - 4x_3^2) (|\Theta|_1^2 - 12x_1^2) \quad (\text{B.16})$$

$$g_{1222} = \frac{1}{24} x_2 (-h_2^2 + 4x_2^2) x_1 \quad (\text{B.17})$$

$$g_{1333} = \frac{1}{24} x_3 (-h_3^2 + 4x_3^2) x_1 \quad (\text{B.18})$$